Identification of a Fe(OH)2-like phase in the core–shell structure of nano-zero-valent Fe and its evolution when interacting with Pd2+aq ions by Mössbauer spectroscopy, XPS, and TEM

Mustapha Abdelmoula, Christian Ruby, M. Mallet, Jaafar Ghanbaja, Romain Coustel, Louis Scudiero, Wei-Jyun Wang

▶ To cite this version:

Mustapha Abdelmoula, Christian Ruby, M. Mallet, Jaafar Ghanbaja, Romain Coustel, et al.. Identification of a Fe(OH)2-like phase in the core–shell structure of nano-zero-valent Fe and its evolution when interacting with Pd2+aq ions by Mössbauer spectroscopy, XPS, and TEM. Journal of Physics and Chemistry of Solids, 2023, 172, pp.111066. 10.1016/j.jpcs.2022.111066 . hal-03893779

HAL Id: hal-03893779

https://hal.science/hal-03893779v1

Submitted on 19 Jan 2023

Submitted to Journal of Physics and Chemistry of Solids

Identification of a $Fe(OH)_2$-like phase in the core–shell structure of nano-zero-valent Fe and its evolution when interacting with Pd^{2+}_{aq} ions by Mössbauer spectroscopy, XPS, and TEM

M. Abdelmoula[a], C. Ruby[a*], M. Mallet[a], J. Ghanbaja[b], R. Coustel[a],
Louis Scudiero[c], Wei-Jyun Wang[d]

[a] Université de Lorraine, CNRS, LCPME, F-54000 Nancy, France
[b] Université de Lorraine, CNRS, IJL, F-54000 Nancy, France
[c] Chemistry Department and Materials Science and Engineering Program, Washington State University, Pullman, WA 99164, USA
[d] The Gene and Linda Voiland School of Chemical Engineering and Bioengineering, Washington State University, Pullman, WA 99164, USA University, Pullman, WA 99164, USA
* Corresponding author: christian.ruby@univ-lorraine.fr
Full postal address: LCPME, 405 rue de Vandoeuvre, 54600 Villers-lès-Nancy, France

Abstract

Synthesized Fe@FeOx nanoparticles (NPs) were fully characterized by spectroscopic techniques and (scanning) transmission electron microscopy to resolve the presence of a $Fe(OH)_2$-like phase. The different phases detected in the core–shell nanostructure of these NPs were corroborated by Mössbauer and X-ray photoelectron spectroscopies. Metallic iron (Fe^0), ferrous (Fe^{II}) hydroxide, magnetite ($Fe^{III}_2Fe^{II}O_4$), and a top layer of ferric (Fe^{III}) oxide were identified. Interestingly, ferrous hydroxide reacted with Pd^{2+}_{aq} upon coating of the supporting core–shell material when Pd was added to produce Fe@FeOx/Pd NPs.

Keywords: Iron, Superparamagnetism, TEM, XPS, TMS, Core–shell

1. Introduction

Zero-valent iron nanoparticles (Fe-NPs) have been synthesized using various methods including (i) ball milling of bulk Fe particles, (ii) reduction of Fe oxides to Fe^0 with hydrogen gas and (iii) aqueous reduction of ferric (Fe^{III}_{aq}) or ferrous (Fe^{II}_{aq}) species [1,2]. In aqueous solution, the most commonly used method is the reduction of ferric species by sodium borohydride ($NaBH_4$) as initially proposed by Wang et al. [3]. In comparison with the classical micrometric-sized Fe^0 granular materials, Fe-NPs present generally higher chemical reactivity due to their higher surface to volume ratio. Fe-NPs have been used to eliminate organic and inorganic pollutants and their efficiency when directly injected in groundwater [4,5]. Furthermore, when the surface of these NPs is modified by organic stabilizers, their agglomeration decreases and their dispersion into the reactive media increases [6]. Additionally, Fe-NPs were used as a substrate to stabilize metallic clusters such as Cu^0 or Pd^0 on their surface [3,7,8]. The preparation of NPs with such modified surfaces was performed relatively easily by reducing Cu^{II} or Pd^{II} salt at the NP–water interface. In addition, metal-coated Fe-NPs where shown to be effective catalyzers to oxidize formate and reduce carbon dioxide to formate [8] or to catalyze the reaction between iodobenzene with benzene boronic acid to form a biphenyl product (Suzuki−Miyaura cross-coupling reactions) [7]. Many core–shell structures containing metals and oxides have been studied for their original magnetic properties (e.g. $Fe_{(1-x)}O/Fe_3O_4$ [9] and Ni/Au [10]) or their electrocatalytic properties (e.g. Pd/Pt [11]). Zero-valent NPs have the advantage of being relatively cheap and ecofriendly NPs with Fe^0 or Fe^{II} redox active species present in their structure. Another important potential application of Fe-NPs free of metallic Fe^0 and containing Fe_3O_4 or maghemite γ-Fe_2O_3, is as materials for the treatment of cancers by magnetic hyperthermia [12–15]. The numerous implications of Fe-based materials in various technological applications make the full characterization of these materials very important.

The nanostructure and physicochemical properties of the Fe-NPs synthesized in the presence of $NaBH_4$ have been studied using several techniques, including X-ray diffraction (XRD) [3,7,8,16–19], scanning electron microscopy (SEM) [16,19,20], high-resolution transmission electron microscopy

(HR-TEM) coupled with energy dispersive X-ray spectroscopy (EDX) or electron energy loss spectroscopy (EELS) [7,8,16–18], atomic force microscopy (AFM) [13], X-ray photoelectron spectroscopy (XPS) [8,17,20], X-ray absorption near edge structure (XANES) [7,17], Raman [18] and Mössbauer spectroscopies [19–21] and finally electrochemically using cycling voltammetry or chronoamperometry [8]. In all these studies the NPs were constituted by a metallic Fe^0 core and a Fe oxide shell. The chemical composition and the phase partition in the core–shell were shown to depend on the synthesis conditions such as the nature of the Fe salt containing either Fe^{II} or Fe^{III} species and the contact time between the Fe salt and the reducing agent $NaBH_4$ [18]. The XRD analyses provide essential information about the structure of the core constituted by metallic bcc Fe [3,7,16–18]. In some studies, very low intensity or broad diffraction peaks attributed to Fe oxides were observed [17]. Nevertheless, XRD is certainly not the most suitable technique to characterize more or less crystalized thin Fe oxide coatings present at the surface of Fe-NPs. The presence of a mixture of Fe^{II} and Fe^{III} species in the shell was clearly shown in XANES and XPS studies [7,8,17]. Using a series of reference samples, Yao et al. [7] estimated the relative proportion of Fe^0, Fe^{II}, and Fe^{III} species in Fe-NPs. The determination of such a speciation was also possible using XPS [8,17], which probes the extreme surface of the analyzed materials (maximal analysis depth < 10 nm). Since the average sizes of the synthesized Fe-NPs were 10–50 nm [7,8,17,18,20], XPS provided a good picture of the chemical composition of the NPs. In addition, such results should be carefully analyzed by considering the various fitting procedures used [22,23]. The unique technique ^{57}Fe Mössbauer spectroscopy is used to determine the mineralogical nature of the Fe-rich phases as well as their relative proportions. Relatively complex Mössbauer spectra of Fe-NPs were recorded at room temperature (RT, 298 K) [19,21]. The complexity of the spectra is directly related to the reduced size of the grains and then their superparamagnetic behavior [24–27]. In all the Mössbauer spectra previously shown, Fe^0 was clearly identified but the exact chemical nature of the Fe oxides present in the shell was not. Moreover, some of the Mössbauer spectra at 298 K exhibited a paramagnetic ferrous doublet that was not fully interpreted [19–21]. Indeed, recording the Mössbauer spectra in a full range of temperatures of 4–298 K is generally required to obtain full characterization of a sample. This characterization has never been done for Fe/FeOx NPs. In our study, a combination of microscopic and spectroscopic techniques – TEM/scanning TEM (STEM) coupled with EELS/X-ray chemical imaging and electron diffraction, XPS and Mössbauer spectroscopy – were used to highlight the nanostructure of Fe-NPs and their evolution when interacting with Pd^{II}_{aq} ions.

2. Materials and methods

2.1. Preparation methods

Iron(II) sulfate heptahydrate ($FeSO_4{\cdot}7H_2O$, 99%), palladium(II) chloride ($PdCl_2$, 99%), polyvinylpyrrolidone (PVP, average molecular weight = 55 000), $NaBH_4$, and glacial acetic acid were purchased from Sigma Aldrich. Hydrochloric acid (HCl, 36.5%) was purchased from J.T. Baker.

The Fe@FeO_x NPs were prepared by mixing 8.0 mL of 0.625 M $FeSO_4{\cdot}7H_2O$ aqueous solution and 10 mL of 2 M PVP methanol solution. The solution was then manually stirred with a glass rod for 1 min. The starting reagents were immediately reduced by adding dropwise 2.0 mL of a 1.82 M $NaBH_4$ aqueous solution. The mixture turned into a thick black liquid that was stirred for 3 min. Finally, 0.15 mL of 0.5 M H_2SO_4 was added, followed by 0.05 mL of 1 M glacial acetic acid to neutralize the remaining $NaBH_4$. The final solution was centrifuged at 3400 rpm and washed with methanol. During the synthesis, solution pH increased from 4.1 to 6.8 and reached a final value of 6.1 at the end of the synthesis.

The Fe@FeO_x/Pd NPs were obtained by dispersing the Fe@FeO_x NPs into methanol and adding 133 µL of 0.5 M H_2PdCl_4. The solution was then shaken for 30 s and sonicated for 30 min to facilitate the galvanic displacement process. The solution was centrifuged at 3400 rpm, rinsed with methanol, and dried in a vacuum desiccator.

2.2. Methods employed for solid characterization

2.2.1. TEM

The TEM and STEM investigations were carried out using a JEM - ARM 200F Cold FEG TEM/STEM (JEOL, Japan) operating at 200 kV, coupled with a GIF Quantum 965 ER (Gatan-Ametek, USA), and equipped with a spherical aberration (Cs) probe and image correctors (CEOS GmbH, Germany). For TEM/STEM observations, one drop of a dispersed solution of NPs was deposited on a carbon-coated copper grid.

2.2.2. XPS

The XPS spectra were recorded on an AXIS Ultra DLD (Kratos Analytical, Ltd) equipped with a monochromatized AlKα X-ray anode at 1486.6 eV (spot size 700 µm × 300 µm). High-resolution spectra were acquired at a pass energy of 20 eV (core level spectra). Charging effects were compensated through low-energy electron flooding. In order to decrease any surface contamination and characterize the chemical composition underneath the surface, sputtering was done using an Ar^+ ion beam energy of 5.05 kV. Data analysis and curve fitting were performed using Casa XPS software. A Gaussian/Lorentzian (70/30) product function and a nonlinear Shirley background were used. Binding energies were calibrated by assigning the adventitious carbon C 1s peak to 284.6 eV. The high-resolution spectra were deconvoluted into the components corresponding to bond types. The chemical state information from the Fe2p core level was obtained following the procedure of Grosvenor et al. [22] to describe the multiplet structure of Fe oxides. Thus, four and three components were used to account for the multiplet structure of Fe^{III} and Fe^{II} bound to O_2, respectively. Additionally, broad peaks at around ~715 and ~720 eV were added to account for the Fe^{II} and Fe^{III} satellites.

2.2.3. Transmission Mössbauer spectroscopy (TMS)

Mössbauer spectroscopy was performed at 297, 130, 77, 38, 16, 10, 7, and 4 K with a constant acceleration Mössbauer spectrometer, 512 multichannel analyzer (Halder Electronic Gmbh), and a 50 mCi source of ^{57}Co embedded in a Rh matrix maintained at RT. Samples were prepared under N_2 atmosphere in an anoxic glove box (Jacomex) using appropriate amounts (10 mg of powder per cm^2)

of solid samples to get optimal experimental conditions. Measurements were recorded in the velocity range of ±11 mm s^{-1}. Analyses were first carried out between ambient temperature and 10 K on the ARS cryostat (Advanced Research Systems, Macungie USA) equipped with a vibration isolation stand developed at LCPME and then for the lowest temperatures of 7.8 and 4 K on a Janis cryostat (SHI-850, Janis Research Co., Wilmington, MA, USA). Mössbauer spectra were collected in transmission mode. The 50 mCi source of ^{57}Co in the Rh matrix was maintained at RT and mounted at the end of a Mössbauer velocity transducer. Both spectrometers were calibrated with a 25-µm foil of α-Fe at RT. Spectra were computer-fitted with the Voigt-based fitting model for paramagnetic sites corresponding to a doublet with a distribution of quadrupole splittings and magnetic sites corresponding to a sextet with a distribution of magnetic hyperfine fields (HFDs), as implemented in Recoil software [28]. Nevertheless, an exception was adopted for the spectra recorded below 10 K where the appearance of a magnetic order for phases containing Fe^{II} species required the full static Hamiltonian site model to solve the mixed hyperfine interactions.

3. Results and discussion

3.1. TEM/STEM-EELS analysis

3.1.1. Characterization of Fe@FeOx NPs

High-angle annular dark field (HAADF) (Z contrast; Z, atomic number) micrographs showed the of the Fe@FeOx NP structure (Fig. 1a). The NPs were mostly spherical in shape, with a core (very bright) and shell (less bright) as previously observed [7]. They also appeared in a chain-like aggregate conformation (Fig. 2). The diameter range of these NPs was ~13–20 nm with a shell thickness of ~3–5 nm (Fig. 1a and b). The bright field (BF)-TEM micrographs and the corresponding selected area electron diffraction (SAED) pattern were also recorded (Fig. SI-1). Very diffuse diffraction rings were obtained, showing that the phase present in the NPs was very poorly crystallized. The TEM results were in very good agreement with the complementary XRD pattern obtained for the Fe@FeOx sample (Fig. SI-2), in which only two very broad diffraction peaks, attributed to the most intense

(110) crystallographic plane of Fe^0 and the (311) crystallographic plane of magnetite, were measured. Fig. 2a exhibits HR-TEM micrographs and a high-resolution micrograph with its corresponding Fast Fourier Transform (FFT). The d-spacings measured on the FFT were 2.60 and 2.06 Å. These values can be attributed to the (311) and (400) crystallographic planes of magnetite. The d-spacing of 2.06 Å could also be attributed to the (110) diffraction plane of α-Fe, meaning that a superposition of the diffraction rings due to the (110) plane of α-Fe and the (400) plane of Fe_3O_4 is also possible. Moreover, HR-TEM micrographs confirmed the layered nanostructure of the shell (Fig. 1b). The STEM-EELS experiments, performed to simultaneously acquire HAADF micrographs for the O-K and Fe-$L_{2,3}$ edges (Appendix A), showed that the core of the NPs contained contributions of both metallic Fe (Fe^0) and Fe oxide (Fe^{II} and Fe^{III}), making the separation between the different phases difficult. The EDX elemental mapping removed this difficulty and the combined elemental mapping for the Fe-$L_{2,3}$ and O-K edges revealed a metallic Fe^0 core (green) and a Fe oxide shell (orange) (Fig. 2). This result was also confirmed by the STEM-EDX line profile on an individual NP (Fig. SI-3).

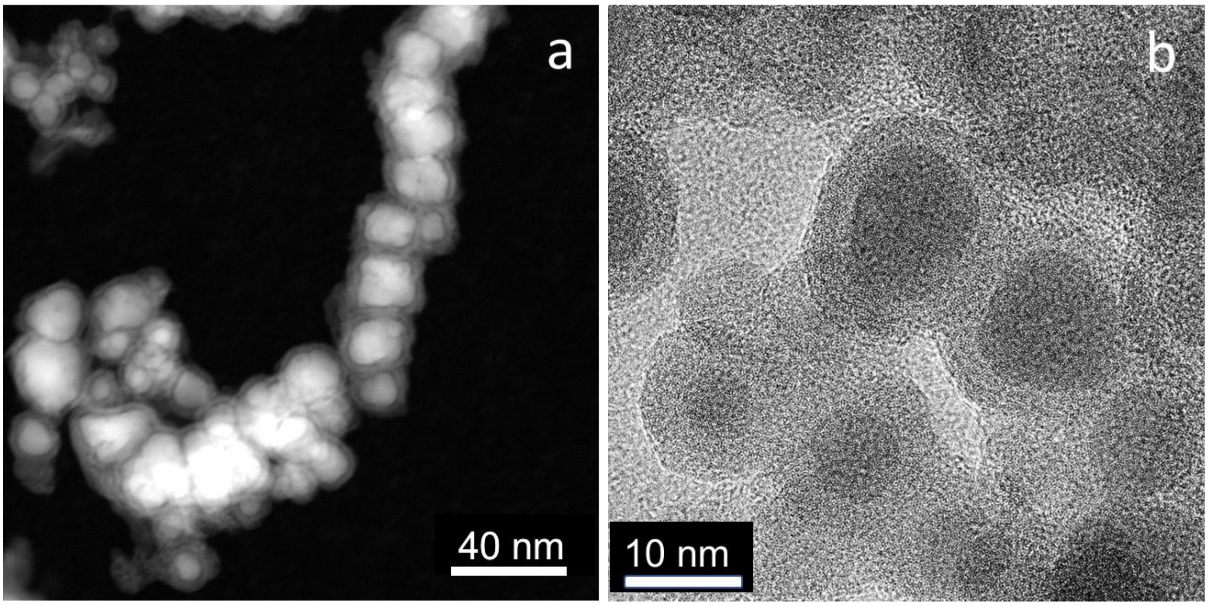

Fig. 1. (a) HAADF-STEM and (b) HR-TEM micrographs of Fe@FeOx nanoparticles.

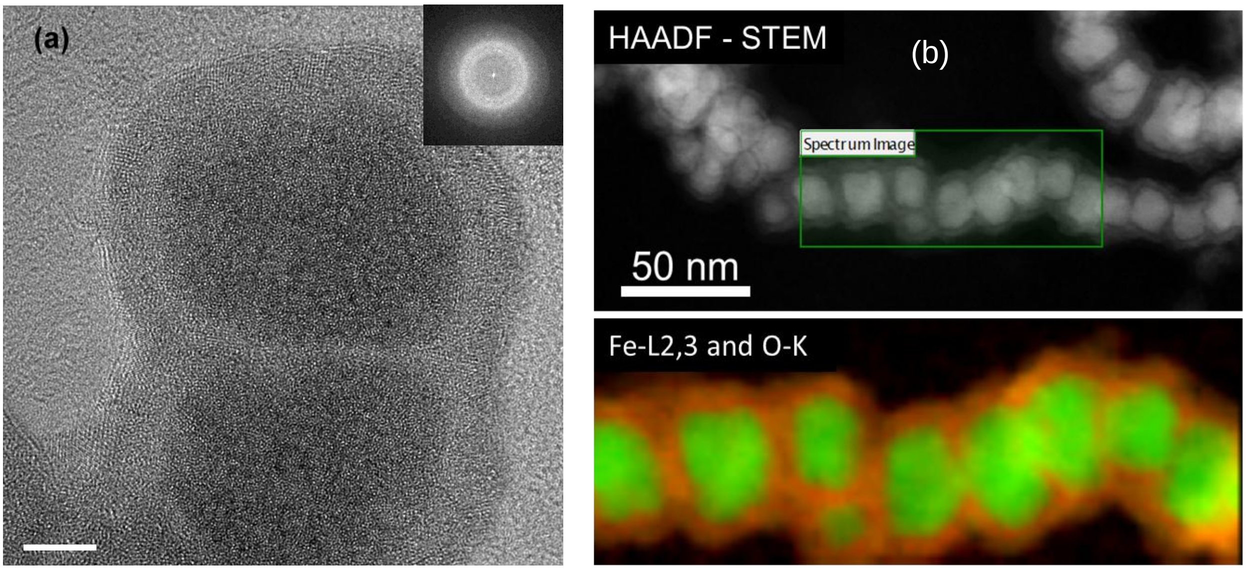

Fig. 2. (a) HR-TEM micrographs of Fe@FeOx sample and its FFT in the inset. (b) HAADF image of Fe@FeOx nanoparticles and corresponding elemental mapping. The zones highlighted in green and orange correspond to Fe-rich and O-rich areas, respectively. The figure was adapted from data of a previous work [8].

3.1.2. Characterization of Fe@FeOx/Pd NPs

The nanostructure of Fe@FeOx NPs exposed to H_2PdCl_4 was studied using TEM and STEM (Fig. 3). The images displayed a heterogeneous distribution of dense NPs forming aggregates of several hundreds of nanometers constituted by grains of about 5 nm (see the dense dark NPs in Zone A in Fig. 3a). A few uncovered core–shell Fe@FeOx NPs were visible (Zone B in Fig. 3a). On one hand, the zones corresponding to the dense NP aggregates were analyzed more specifically and the corresponding FFT pattern displayed rings with *d*-spacings typical of fcc metallic Pd^0 (Fig. 3b). Additionally, STEM-X-ray mapping was performed (Fig. 4). The analysis showed that both Pd and Fe were present in the aggregates of zone A (~80 at.% of Pd and ~20 at.% of Fe). On the other hand, analysis of the diffraction pattern for areas containing uncoated core–shell Fe@FeOx NPs (Zone B) revealed the presence of magnetite (FFT similar to that recorded in Fig. 2a).

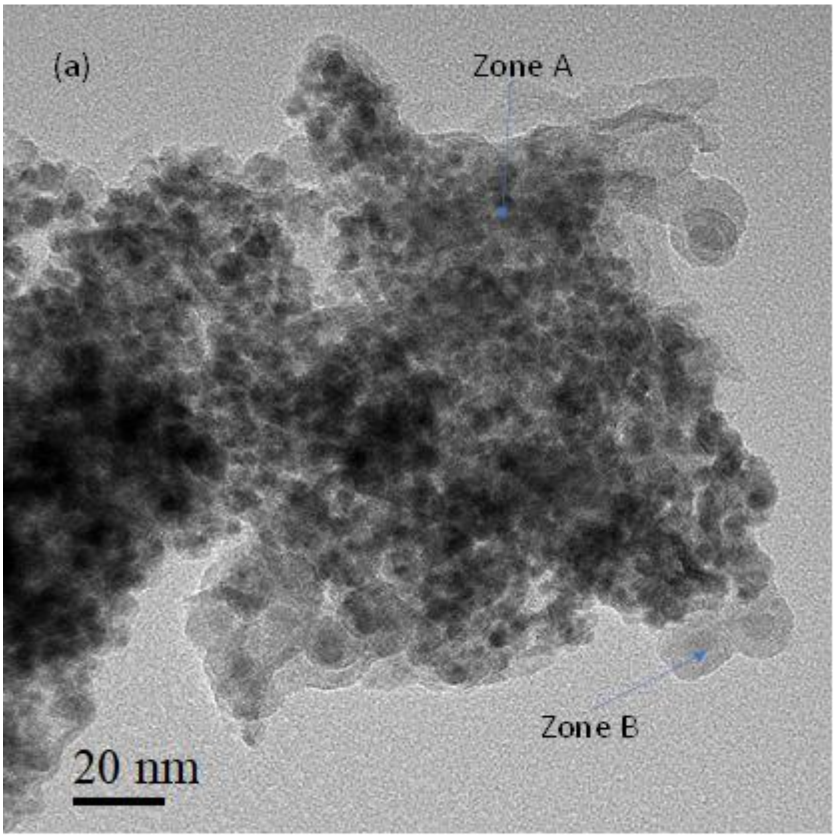
(a)
Zone A
Zone B
20 nm

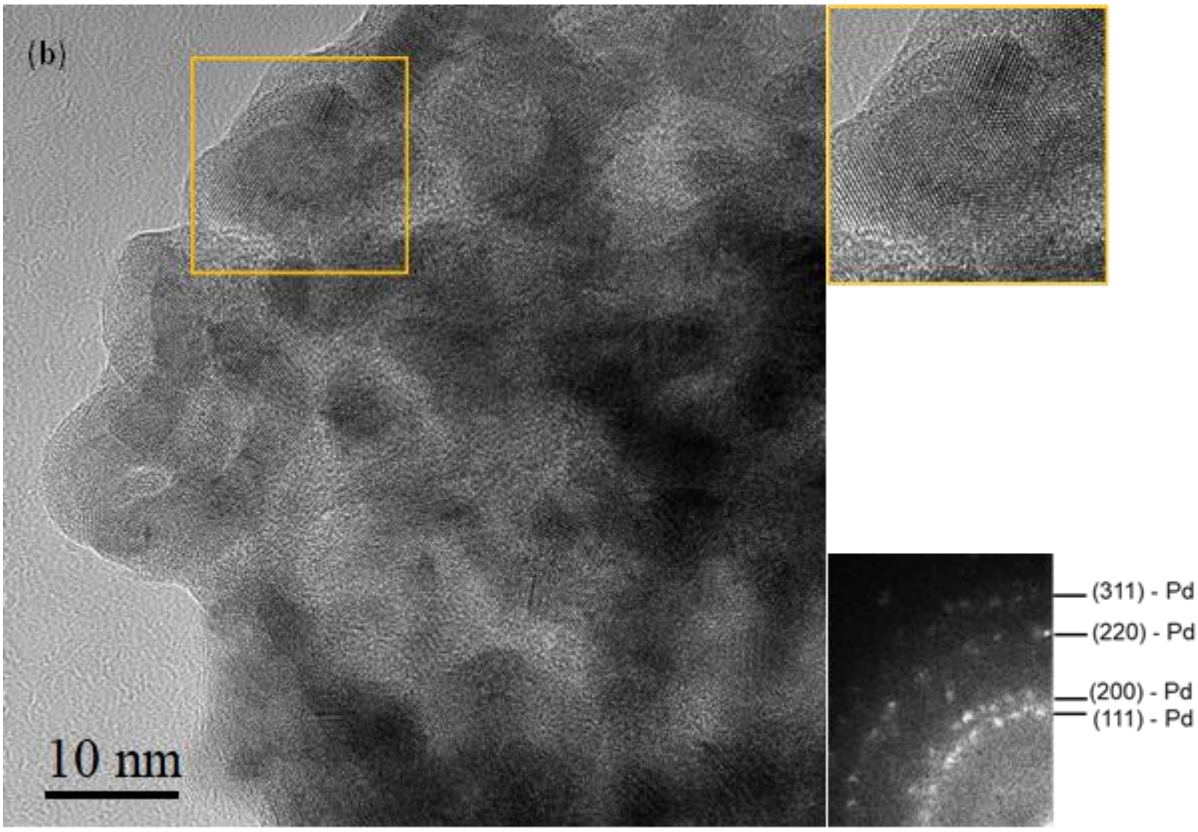
(b)
10 nm
(311) - Pd
(220) - Pd
(200) - Pd
(111) - Pd

Fig. 3. (a) Typical BF-TEM micrograph showing Pd-rich zones (Zone A) and uncovered core–shell Fe@FeOx NPs (Zone B). (b) HR-TEM micrograph and corresponding FFT recorded in a Pd-rich zone (Zone A). The indexation of the Pd^0 diffraction rings is also given.

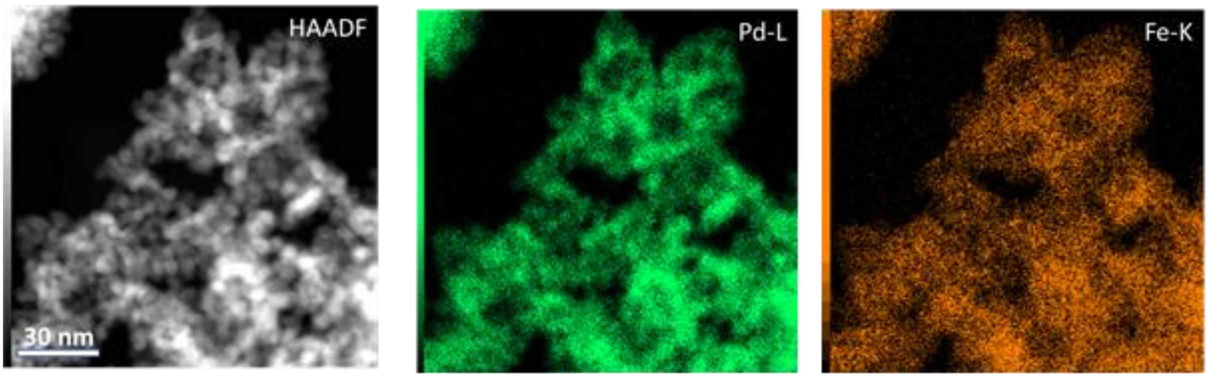

Fig. 4. STEM X-ray mapping of the Fe@FeOx/Pd NPs in a Pd-rich zone (Zone A).

3.2. XPS analysis

3.2.1. Characterization of Fe@FeOx NPs

An XPS analysis provides valuable information about the chemical composition of a sample and chemical bonding of atoms from the surface of a material. The surface quantitative elemental composition determined by XPS before and after Ar$^+$ sputtering is reported in Table 1. As expected, Fe, oxygen (O), and carbon (C) were present in Fe@FeOx NPs. The Ar$^+$ sputtering decreased the C contribution and increased that of Fe, while the amount of O was not significantly affected. Due to the spin-orbit j–j coupling, the Fe 2p core levels split into 2p$_{1/2}$ and 2p$_{3/2}$ components, situated at ~710.2 and ~723 eV, respectively (Fig. 5a). In addition, there was a relatively strong satellite peak in the 718–720 eV region, which is characteristic of a Fe^{III}-rich surface (Fig. 5a). The deconvolution of the Fe 2p$_{3/2}$ region was performed with contributions from Fe^0 (706.7 eV), Fe^{II} (708.5–710.5 eV), and Fe^{III} (710.1–713.5 eV) [22,23]. This fitting procedure allowed the determination of the relative proportion of Fe^0, Fe^{II}, and Fe^{III} species present on the surface of Fe@FeOx NPs (Table 1). A relative proportion as high as ~85% of Fe^{III} species was found, with much lower proportions of Fe^{II} and Fe^0 of around 11% and 4%, respectively. The relatively low concentration of Fe^0 can be easily understood since the Fe^0 core is covered by a relatively thick oxide layer (3–5 nm) of magnetite (Fig. 6a), as previously observed using TEM (Fig. 1b). The magnetite top layer showed a Fe^{III}/Fe^{II} ratio of 7.7 and then appeared to be partially oxidized into a very thin layer of Fe^{III}-rich oxides, most likely an epitaxial layer of maghemite γ-Fe_2O_3. The Ar^+ sputtering partially removed both the C contamination and the γ-Fe_2O_3 top layer (Fig. 6b). Fig. 5b displays a Fe 2p spectrum with characteristics much closer than the reference spectra of magnetite synthesized under ultra-vacuum [29,30]. In particular, the detection of a much higher concentration of Fe^{II} species (~48%, Table 1) correlates well with the presence of a strong satellite peak around 716 eV in the Fe 2p spectrum (Fig. 6b). Note that the ratio Fe^{III}/Fe^{II} of 1 measured after Ar^+ sputtering was significantly lower than the expected value of 2 corresponding to stoichiometric magnetite $Fe^{III}_2Fe^{II}O_4$. This result may be attributed to the coexistence of a Fe^{II}-rich extra-phase beside magnetite, which is in good agreement with the Mössbauer results presented later in section 3.3.

Sample	**Elemental composition (at.%)**					**Proportion of iron species (at.%)**		
	Fe	O	Pd	C	Fe/O	Fe(0)	Fe(II)	Fe(III)
Fe@FeOx	*9.4*	*44.3*	-	*46.3*	*0.21*	*3.6*	*11.1*	*85.3*
Fe@FeOx after 4 min Ar^+ sputtering	*18.1*	*45.9*	-	*36.0*	*0.39*	*4.0*	*48.2*	*47.8*
Fe@FeOx/Pd	*3.2*	*41.1*	*7.0*	*48.7*	*0.08*	*1.8*	*22.6*	*75.6*
Fe@FeOx/Pd after 4 min Ar^+ sputtering	*8.0*	*39.6*	*11.9*	*40.5*	*0.2*	*7.6*	*47.0*	*45.4*

Table 1 Relative elemental composition (at.%) and iron speciation determined from XPS analysis.

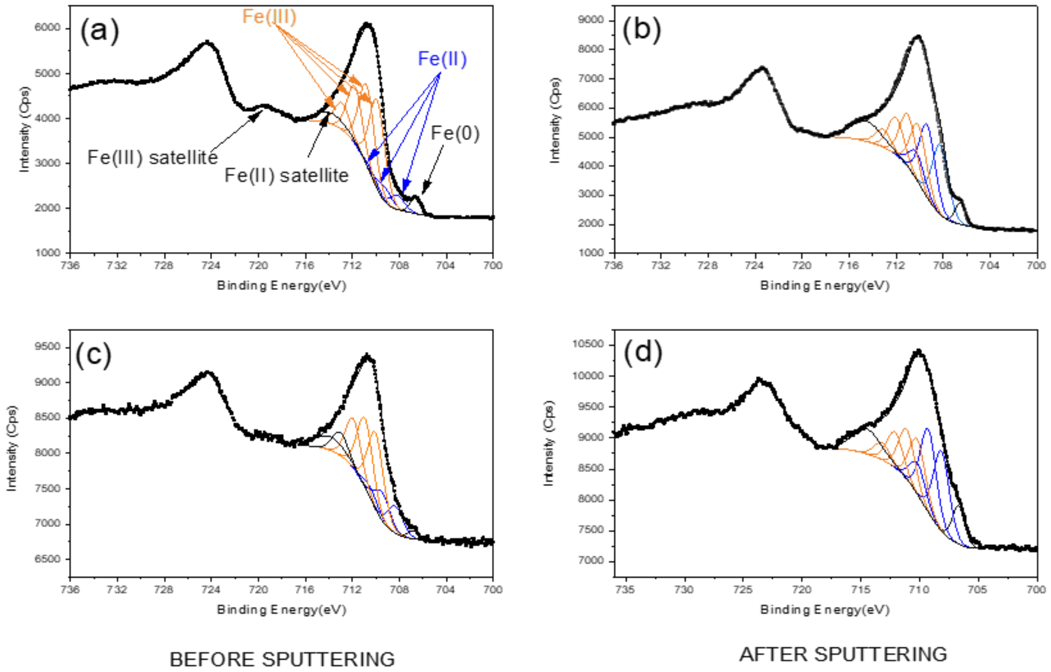

Figure 5: Fe2p XPS spectra of various NPs: (a) Fe@FeOx as prepared (before sputtering), (b) Fe@FeOx after a short Ar$^+$ sputtering, (c) Fe@FeOx/Pd as prepared and (d) Fe@FeOx/Pd after a short Ar$^+$ sputtering. The spectra were adjusted by a procedure using various multiplets as described previously [22-23].

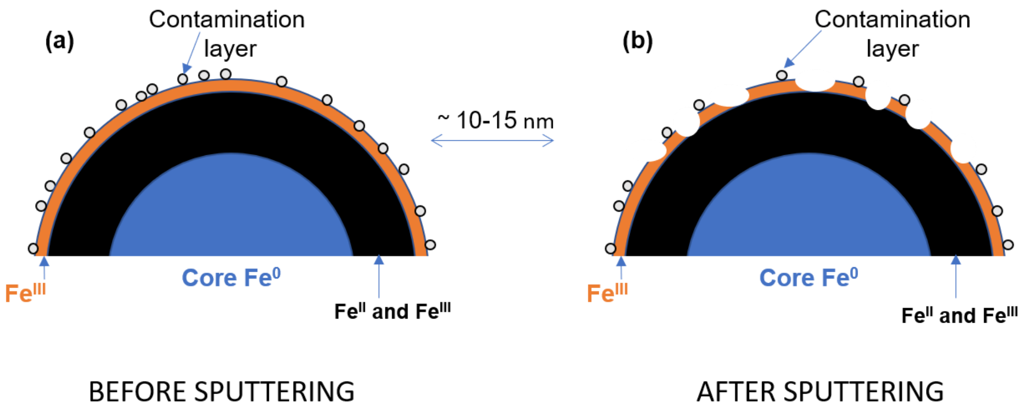

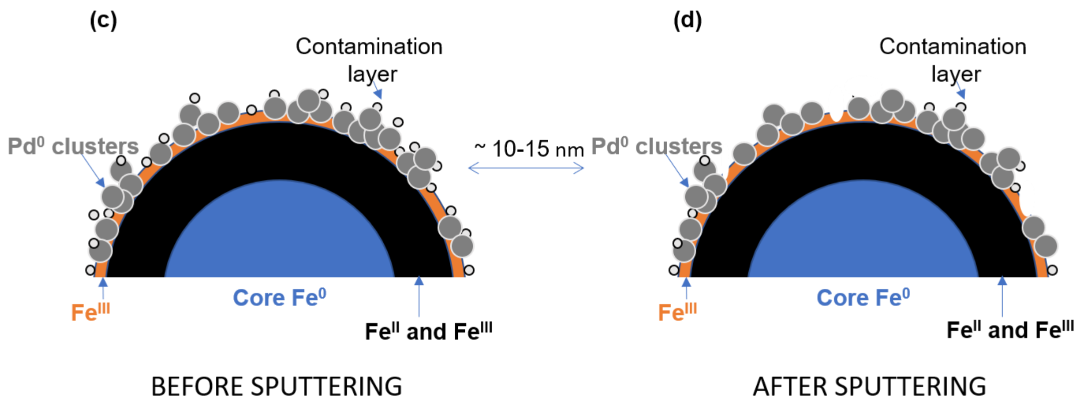

Fig. 6. Schematic view of the NP surface. Fe@FeOx NPs (a) before and (b) after Ar$^+$ sputtering. Fe@FeOx/Pd NPs (c) before and (d) after Ar$^+$ sputtering.

3.2.2. Characterization of Fe@FeOx/Pd NPs

Consistent with the TEM results, XPS measurements indicated that Fe@FeOx NPs showed Pd in addition to C, O, and Fe atoms (Table 1). The Pd 3d$_{5/2}$ peak position was at a binding energy of 335.5 eV, confirming the presence of metallic Pd^0. The presence of Pd^0 aggregates also induced a significant decrease in the relative abundance of Fe by a factor of ~3 (from 9.4% to 3.2%, Table 1). Such a decrease was used to estimate the thickness (T_{Pd}) of the Pd coating according to the following equation:

$$T_{Pd} = - \lambda \times \ln \left(I[Fe]_c \,/\, I[Fe]_0 \right) \qquad \text{Eq. 1}$$

where λ is the inelastic mean free path of the Fe 2p electrons (λ ~ 1 nm [31]), $I[Fe]_c$ is the relative abundance of Fe recorded for the substrate coated with a top layer of Pd^0 of thickness (T_{Pd}), and $I[Fe2p]_0$ is the relative abundance of Fe 2p recorded for the uncovered substrate (T_{Pd} = 0 nm).

An estimated thickness of Pd^0 of ~1 nm was computed using Eq. (1), derived for a uniform coating on a flat surface. The obtained value should therefore be considered a very rough estimation of the Pd^0 coating thickness (within an order of magnitude). The TEM showed that the deposited Pd^0 did not form a uniform coating but rather clusters (Fig. 3a), therefore the actual Pd^0 thickness was certainly higher or lower than ~1 nm. A schematic representation of these Pd^0 clusters before and after Ar^+ sputtering is given in Fig. 6c and d. The sputtered Fe@FeOx/Pd NPs was characterized by a higher concentration of Fe^{II} species in comparison with the as-prepared Fe@FeOx NPs (before sputtering). As observed for Fe@FeOx NPs, the Ar^+ sputtering led to a significant decrease of the C and Fe^{III} contents and a Fe^{II}/Fe^{III} ratio of ~1 was determined.

3.3. TMS analysis

3.3.1. Relaxation phenomena and characterization of Fe@FeOx NPs

In a first step, the Mössbauer spectra were recorded in a temperature range from RT to 10 K (Fig. 7). A general feature was the shape of Mössbauer spectra characterizing the presence of magnetic relaxation with two regimes: one above and one below 77 K. The term relaxation covers different phenomena subject to various terms, i.e. time-dependent and (or) also temperature-dependent phenomena. Two characteristic times are generally considered in Mössbauer spectroscopyy: (i) the mean life time of the excited nuclear level (100 ns), which determines the resolution of the spectra, and (ii) the inverse of the nuclear Larmor precession frequency, which is the frequency at which the magnetic moment of the nucleus precesses (~34 MHz) in the HFD. When an isolated magnetic particle is small enough, its magnetic moment (the macro spin) fluctuates between the easy directions of magnetization. The characteristic time of such a fluctuation is designated as the “flip” time and corresponds to the inverse of the transition rate. The Mössbauer spectrum of such a particle strongly depends on the ratio between the transition rate and the Larmor frequency. If the “flip” time of the magnetic moment of the particle is much longer than the nuclear Larmor precession period, then the nucleus feels the magnetic field due to the electronic cloud (particle magnetic moment) and interacts with it through its nuclear magnetic moment (Zeeman splitting). In this situation, the obtained Mössbauer spectrum present a magnetic structure. On the contrary, if the “flip” time of the magnetic moment of the particle is much shorter than the nuclear Larmor precession period, the nucleus perceives a zero (time-average) particle magnetic moment. The latter situation prevents the observation of a magnetic structure in the Mössbauer spectrum, which corresponds to superparamagnetic relaxation. Among principal types of relaxation, superparamagnetism in small magnetic particles became the subject of several publications [23–27]. In particular, Mössbauer spectroscopy was shown to be extremely sensitive to some of the size-dependent properties of very small particles.

In the first temperature range from RT to 77 K, spectra were fitted with two (or three) quadrupole doublets D1, D2 (or D3), and two (or three) sextets. The detailed values of the hyperfine parameters of the components used to fit the Mössbauer spectra recorded for Fe@FeOx NPs were provided (see Appendix B, Table B-1). Doublet D1 was characterized by large CS and Δ values of 1.28 and 2.10 mm s^{-1}, respectively. The value of Δ and its increase with lowering temperature is typical of a Fe^{II} state in an octahedral site.

At RT, another paramagnetic component was reasonably described as a superimposition of elemental sub-spectra D2 and D3 whose hyperfine parameters differed from those of the ferrous doublet. The spectrum of a magnetic component constituted by two sextets (S1 and S2) was also observed. Sextets S1 and S2 could be ascribed to the components of a superparamagnetic magnetite whose HFDs are reduced with respect to bulk magnetite. Superparamagnetic relaxation was the most important determining factor for the temperature dependence of spectra due to the range of particles size as measured by TEM. Indeed, the Morup model [23] developed for studying the Mössbauer spectra of NPs explained the reduction of the HFDs with asymmetric and broad lines.

At 130 K, doublet D2 disappeared and an additional broad sextet appeared with lower HFD than those of S1 and S2. The superposition of D2 and D3 at RT with the transformation from D2 to S3 at 130 K corresponded to metallic Fe-NPs that present superparamagnetic behavior. Doublets D2 and D3 (or D3 and S3 with a low HFD) were obtained to the detriment of the classical α-Fe sextet characterized by a HFD of 329 kOe. The presence of paramagnetic doublets was observed in a previous study of ultrathin pure ^{57}Fe (thickness lower than one monolayer) prepared under ultrahigh vacuum [32]. In the temperature range of 38 to 10 K, the line shapes were poorly evolved compared to those obtained between ambient temperature and 77 K. One should note that the CS value of 0.78 mm s^{-1} obtained for the Fe^0 sextet at 38 K was much higher than the expected value of 0.12 mm s^{-1}. Such a discrepancy could be due to the complexity of our fitting procedure using multiple components.

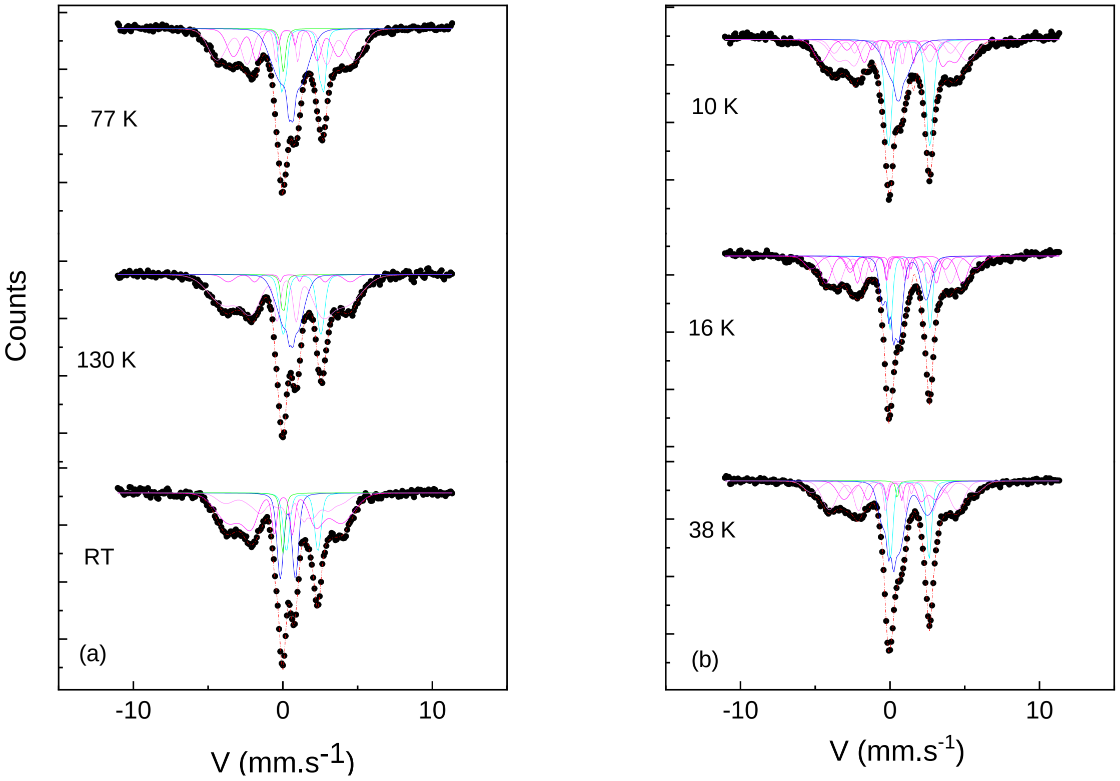

Fig. 7. Mössbauer spectra for Fe@FeOx NPs recorded between room temperature and 10 K. (a) Solid black circles, experimental curve; dash dot line in red, global computed curve; solid line, sub-components of the spectra; cyan, D1 associated with Fe(II) in $Fe(OH)_2$; green and blue, D3 and D2 (or sextet) associated with Fe(0), respectively; magenta, sextets S1 and S2 associated with magnetite.

(b) Solid black circles, experimental curve; dash dot line in red, global computed curve; solid line, sub-components of the spectra; cyan, D1 associated with Fe(II) in $Fe(OH)_2$; blue, sextet associated with Fe(0); magenta, sextets S1 and S2 associated with magnetite.

The global shape of the spectra recorded at temperatures of 7.8 and 4 K (Fig. 8) completely differed from those recorded above 10 K. The adjustment of such spectra was relatively complex and may not be unique. Here, seven components were used to properly fit the experimental spectra. Six sextets were necessary to reproduce the magnetite contribution. Metallic Fe (Fe^0) NPs gave rise to one sextet (green line). Moreover, according to literature [33], at low temperature, microcrystalline magnetite requires five sextets – attributed to one Fe^{III} located in tetrahedral sites, two Fe^{III} in octahedral sites, and two Fe^{II} in octahedral sites. In addition, the calculated HFDs were much lower than expected for microcrystalline magnetite. The effects of apparent reduction of the HFD as a function of temperature or volume of the crystallites were widely debated in various theoretical models [23–27,34]. These effects were combined and explained by two phenomena: (i) the proportion of surface atoms and (ii) the fluctuation of the magnetization due to the interactions between particles. Finally, the Fe^{II} species observed in a paramagnetic state between 300 and 10 K were described with an octet (cyan line) corresponding to a magnetically-ordered Fe^{II} phase below 10 K. The electric quadrupole interaction cannot be treated as a perturbation of the Zeeman splitting [35,36], and it was not possible to analyze the spectra in terms of six-line patterns (sextets) as in the case of the magnetism of ferric components. Therefore, the sub-spectrum comprising eight lines was fully computed by solving the eigenvalues of the Hamiltonian (but only four lines were observable due to the overlap of some transitions). The hyperfine parameters of this octet (Table B-2) were in agreement with some of the features of ferrous hydroxide [$Fe(OH)_2$] [37]. In particular, the HFD of this octet characterized by a value of 160 kOe was comparable to that measured previously for microcrystalline $Fe(OH)_2$ (220 kOe), which underwent a magnetic phase transition from paramagnetic to an antiferromagnetic state below the Néel temperature of 34 K. However, the quadrupole splitting values reported for the Fe^{II} doublet in the temperature range of 300 to 12 K were significantly lower than that previously reported for bulk Fe(OH)$_2$ at 90 K (QS = 3 mm s^{-1} [36]). The origin of this difference between the nanosized “Fe(OH)$_2$-like” phase and bulk Fe(OH)$_2$ is still unclear and needs further investigation.

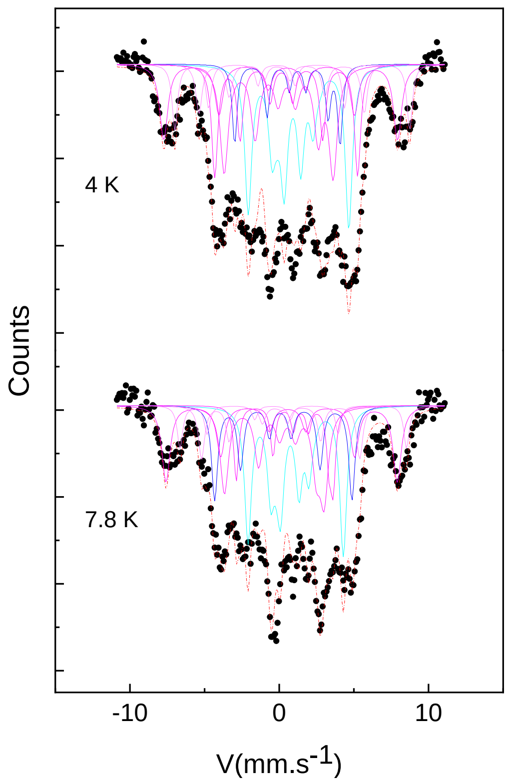

Fig. 8. Mössbauer spectra for Fe@FeOx NPs recorded at 7.8 and 4 K. Solid black circles, experimental curve; dash dot line in red, global computed curve; solid line, sub-components of the spectra; cyan, octet associated with Fe(II) in Fe(OH)$_2$ magnetically ordered; blue, sextet associated with Fe(0); magenta, sextets S1–S5 associated with magnetite.

3.3.2. Characterization of Fe@FeOx/Pd NPs

The Mössbauer spectra at RT, 35 K, and 4 K for the Pd-coated NPs were measured (Fig. 9). The RT spectrum was easily fitted with two doublets and one singlet. In contrast to the sample without Pd, a doublet corresponding to a pure ferrous site was not observed. At 35 K, there was a significant change from a sharp quadrupole doublet to a central broad line. This central line was deconvoluted by three sextets with weak magnetic fields and two small remaining paramagnetic doublets. This transition can be attributed to the dynamic effect resulting from the fluctuations in the local environment of the probe nucleus (^{57}Fe), such as those arising from superparamagnetism. This was confirmed by the line shapes of the spectrum recorded at 8 K, which evolved gradually to a six-line spectrum. At this last temperature, the spectrum exhibited complex magnetic interactions due to the presence of multiple components. The fitting displayed one residual doublet (8% of relative abundance) and six sextets, among which one corresponded to α-Fe (15% of relative abundance) and five components assigned to magnetite (77%). As specified above, the center shift and the hyperfine magnetic fields (Table B-3) deviated from those tabulated for α-Fe components and magnetite. These results confirmed the superparamagnetism behavior as expected for NPs.

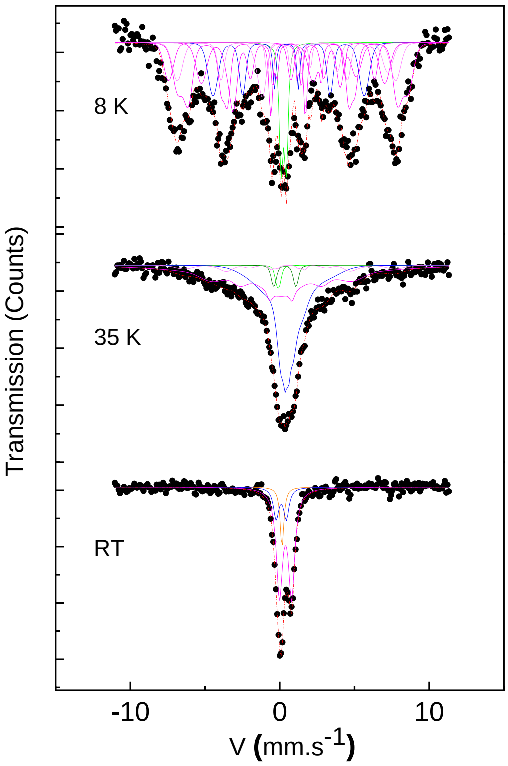

Fig. 9. Mössbauer spectra of Fe@FeOx/Pd NPs at various temperatures. Solid black circles, experimental curve; dash dot line in red, global computed curve; solid line, sub-components of the spectra. Spectrum recorded at room temperature (RT); orange, singlet associated with superparamagnetic phase; blue, doublet associated with Fe(0); magenta, doublet associated with superparamagnetic phase. Spectrum recorded at 35 K; green, doublet associated with superparamagnetic phase; blue, broad sextet associated with Fe(0); magenta, sextets associated with magnetite. Spectrum recorded at 8 K; green, doublet associated with superparamagnetic phase; blue, sextet associated with Fe(0); magenta, sextets S1–S5 associated with magnetite.

3.4. Identification and proportion of the phases present in Fe@FeOx and Fe@FeOx@Pd NPs

The characterization techniques used in this study gave us valuable complementary information about the nature of the phases present in our NPs. The TEM electron diffraction patterns showed that the shell of the Fe@FeOx NPs was mainly constituted by magnetite and the coating of Fe@FeOx/Pd NPs was Pd^0. Metallic Fe^0 was identified in both Fe@FeOx and Fe@FeOx/Pd NPs by XPS, confirming that the shell was mainly composed of a mixture of Fe^{II} and Fe^{III} species. Moreover, the extreme surface of magnetite was constituted by a Fe^{III}-rich phase, most probably a very thin layer of γ-Fe_2O_3. The ^{57}Fe TMS is a unique technique that can determine the nature and relative proportion of the phases. Our measurements identified magnetite, metallic Fe^0, and a $Fe(OH)_2$-like phase Fe@FeOx NPs. Compared to the much more stable γ-$Fe_2O_{3.}$ or Fe_30_4 phases, $Fe(OH)_2$ is an air-sensitive phase and is unstable at the surface of the shell. It is most likely that this $Fe(OH)_2$-like phase could be stabilized at the Fe^0–Fe_3O_4 interface if protected from air; its disappearance as measured by TMS confirmed the very high reactivity of the $Fe(OH)_2$ phase. One may hypothesize that the reduction of Pd^{II}_{aq} ions to Pd^0 was due to an electron transfer between $Fe(OH)_2$-like phase and Pd^{II}_{aq} via the conductive external layer of Fe_3O_4. Interestingly, the radius of the spherical NPs was on average two times that of the core, meaning that the dimension of the core radius was close to the thickness of the shell. As detailed in Appendix C, the volume of the shell was about seven times the volume occupied by the atoms in the core. Note that this ratio of seven is independent of the size of the NPs. Knowing the atomic density of the Fe atoms in magnetite (0.041 At. $Å^{-3}$) and Fe^0 (0.085 At. $Å^{-3}$), a ratio Fe shell/Fe core of ~3.4 was computed. This means that the core contained ~22% of the Fe atoms, a value comparable to the relative proportion of Fe^0 (~15%) derived from Mössbauer spectroscopy at very low temperature (4 K). Therefore, phase proportions derived from TEM or TMS measurements on Fe@FeOx were quantitatively consistent. Note also that the relative proportion of Fe^0 determined in this study (~15%) is in good agreement with that measured by Kanel et al. (~19%) [20] and this relative proportion did not vary significantly after contact with Pd^{II}_{aq} (Appendix B). In fact, the quantity of Fe atoms present in the Fe-NPs (~5 × 10^{-3} moles) was in significant excess compared to the quantity of Pd^{II}_{aq} introduced in the medium (~0.067 × 10^{-3} moles). Therefore, only the specific reactive Fe species, in our case the Fe^{II} species present in $Fe(OH)_2$-like phase, was oxidized. However, note that the Fe^{III}/Fe^{II} ratio measured by XPS did not increase significantly after covering the NPs with Pd^0 (Table 1) as would be expected from the interpretation of the Mössbauer data. This observation could be related to the difference in analysis depth between both techniques or to an eventual preferential Ar^+-sputtering effect. Moreover, by assuming that only the $Fe(OH)_2$-like phase was involved in the reduction of the Pd^{II}_{aq} to Pd^0, the thickness of the Pd^0 coating can be estimated (Appendix C). The values obtained for Pd^0 coating were quasi-linearly dependent on the radius (R_c) of the Fe^0 core. The R_c values of 5–30 nm yielded Pd^0 thicknesses of ~0.1–0.53 nm (Eq. C-1 in Appendix C), consistent with the mean thickness of Pd^0 of ~1 nm estimated using XPS.

4. Conclusion

Mössbauer spectroscopy and XPS were used to determine the nature of the phases present in the core–shell nanostructure of Fe@Fe0x NPs. Metallic Fe^0, a $Fe(OH)_2$-like phase, magnetite, and a top layer of ferric oxides were identified. Interestingly, the $Fe(OH)_2$-like phase was fully transformed when the Fe@Fe0x NPs reacted with Pd^{II}_{aq} and concomitantly the proportion of Fe^0 did not vary significantly. The relative proportion of Fe species present in the core and the shell was revealed by TEM images and determined quantitatively by Mössbauer spectroscopy using the full temperature range of 4–298 K.

Declaration of Competing Interest

The authors declare that they have no known competing financial interests or personal relationships that could have appeared to influence the work reported in this paper.

Acknowledgments

We would like to thank Jason Levy DeMers from Washington State University for his contributions in measuring the pH values at each step of the synthesis of the NPs. Aurélien Renard (Université de Lorraine) is acknowledged for his help with the XPS measurements. The Mössbauer spectroscopy and XPS experiments were supported by means of the Spectroscopy and Microscopy Core Facility of SMI LCPME (Université de Lorraine, CNRS, LCPME- http://www.lcpme.cnrs-nancy.fr), which is gratefully acknowledged.

Appendixes

Appendix A

Fig. A-1. EELS analysis of the (a) core and (b) shell of Fe@FeOx NPs.

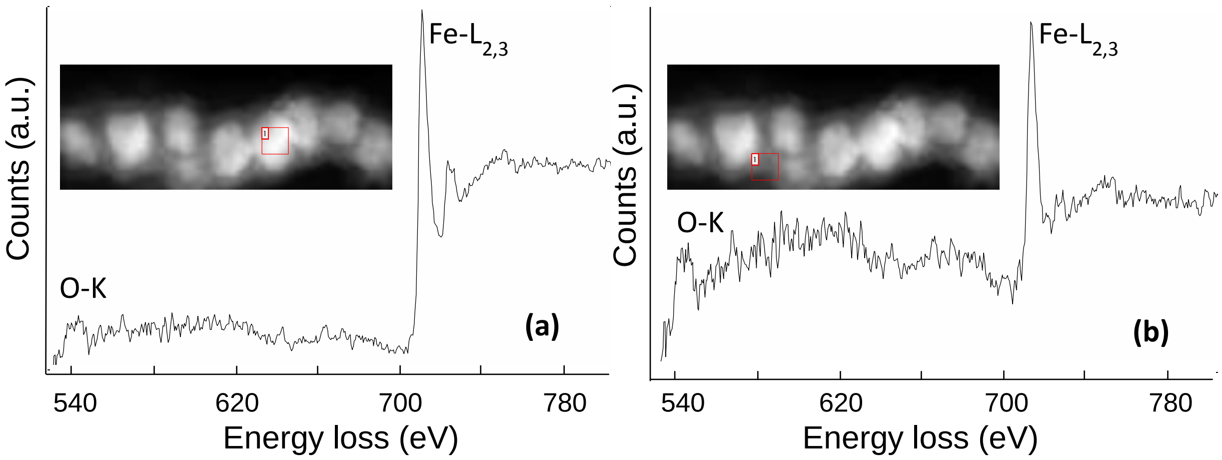

Appendix B

Table B-1 Hyperfine parameters of the Mössbauer spectra of Fe@FeOx NPs at different temperatures recorded on the ARS instrument (see experimental section 2.2.3). CS, Δ, ε, H, and RA are the center shift, quadrupole shift, quadrupole splitting, hyperfine field, and relative abundance of components, respectively.

T = 298 K

Component	**CS (mm s^{-1})**	**Δ or ε (mm s^{-1})**	**H (kOe)**	**RA (%)**
D1: Doublet Fe(II)	1.28	2.1		12
D2: Doublet Fe(0)	0.33	1.01		18
D3: Doublet Fe(0)	−0.002	0.15		4
S1: sextet	0.41	−0.4	172	24
S2: sextet	0.08	0.05	237	42

T = 130 K

Component	**CS (mm s^{-1})**	**Δ or ε (mm s^{-1})**	**H (kOe)**	**RA (%)**

D1: Fe(II)	1.28	2.50		15
D3: Fe(0)	0.03	0.20		3
S1: Sextet 1	0.44	-0.02	253	5
S2: Sextet 2	0.20	-0.05	250	54
Sextet: Fe(0)	0.50	-0.04	47	22

T = 77 K

Component	**CS (mm s^{-1})**	**Δ or ε (mm s^{-1})**	**H (kOe)**	**RA (%)**
D1: Doublet Fe(II)	1.32	2.62		14
D3: most probably Fe(0)	0.03	0.19		4
Sextet	0.24	0.02	218	20
Sextet	0.24	-0.03	285	32
Sextet Fe(0)	0.55	-0.04	56	30

T = 38 K

Component	**CS (mm s^{-1})**	**Δ or ε (mm s^{-1})**	**H (kOe)**	**RA (%)**
D1: Doublet Fe(II)	1.32	2.58		14
D3: most probably Fe(0)	0.48	0.19		1
Sextet: magnetite	0.15	-0.14	190	15
Sextet: magnetite	0.29	-0.07	264	26
Sextet: Fe(0)	0.78	0.71	63	33
Sextet: magnetite	0.40	-0.16	339	11

T = 16 K

Component	**CS (mm s^{-1})**	**Δ or ε (mm s^{-1})**	**H (kOe)**	**RA (%)**
D1: Doublet Fe(II)	1.34	2.66		14
Sextet: magnetite	0.28	-0.14	174	9
Sextet: magnetite	0.34	-0.04	233	19
Sextet: most probably Fe(0)	0.74	0.68	61	29
Sextet: magnetite	0.37	-0.09	283	18
Sextet: magnetite	0.38	-0.14	341	11

T = 10 K

Component	**CS (mm s^{-1})**	**Δ or ε (mm s^{-1})**	**H (kOe)**	**RA (%)**
D1: Doublet Fe(II)	1.35	2.66		16

Sextet: magnetite	0.34	-0.02	197	12
Sextet: magnetite	0.27	0.11	249	13
Sextet: Fe(0)	0.80	0.89	56	30
Sextet: magnetite	0.21	-0.22	295	16
Sextet: magnetite	0.95	-0.13	300	12

Table B-2 Hyperfine parameters of the Mössbauer spectra of Fe@FeOx NPs at different temperatures recorded on the Janis instrument (see experimental section 2.2.3). CS, Δ, ε, H, and RA are the center shift, quadrupole shift, quadrupole splitting, hyperfine field, and relative abundance of components, respectively.

T = 7.8 K

Component	**CS (mm s^{-1})**	**Δ or ε (mm s^{-1})**	**H (kOe)**	**RA (%)**
Octet: Fe(II)	0.90	2.11	159	27
Sextet: magnetite	0.91	-1.09	201	9
Sextet: Fe(0)	0.17	0.21	285	15
Sextet: magnetite	0.36	-0.40	480	16
Sextet: magnetite	0.11	-0.88	207	19
Sextet: magnetite	0.25	1.38	470	6
Sextet: magnetite	0.09	0.38	328	8

T = 4 K

Component	**CS (mm s^{-1})**	**Δ or ε (mm s^{-1})**	**H (kOe)**	**RA (%)**
Octet: Fe(II)	1.10	2.40	162	27
Sextet: magnetite	0.89	-0.68	218	9
Sextet: Fe(0)	0.30	0.31	296	15
Sextet: magnetite	0.30	-0.40	486	14
Sextet: magnetite	0.23	-0.50	226	20
Sextet: magnetite	0.34	1.05	487	8
Sextet: magnetite	0.01	0.30	343	7

Table B-3 Hyperfine parameters of the Mössbauer spectra of Fe@FeOx/Pd NPs at different temperatures. CS, Δ, ε, H, and RA are the center shift, quadrupole shift, quadrupole splitting, hyperfine field, and relative abundance of components, respectively.

T = 298 K

Component	CS (mm s^{-1})	Δ or ε (mm s^{-1})	H (kOe)	RA (%)
Singlet	0.15			12
Doublet: superparamagnetic magnetite	0.38	0.81		70
Doublet: superparamagnetic Fe(0)	0.10	0.69		18

T = 35 K

Component	CS (mm s^{-1})	Δ or ε (mm s^{-1})	H (kOe)	RA (%)
Doublet	-0.10	0.21		2
Doublet	0.33	1.47		3
Sextet	0.59	0.11	88	46
Sextet	0.10	0.02	206	43
Sextet	0.60	0.05	372	6

T = 8 K

Component	CS (mm s^{-1})	Δ or ε (mm s^{-1})	H (kOe)	RA(%)
	0.26	0.35		8
Sextet: magnetite	0.71	0.15	455	27
Sextet: magnetite	0.68	0.20	328	22
Sextet: Fe(0)	0.51	0.07	313	15
Sextet: magnetite	0.37	0.07	452	11
Sextet: magnetite	2.16	0.78	265	8
Sextet: magnetite	0.46	-3.07	299	10

Appendix C

Let us consider a spherical core–shell $Fe^0@FeO_x$ particle as schematized in Fig. C-1 with:

R_C, the radius of the core sphere (Fe^0)

T_S, the thickness of the FeO_x shell

$V_C = \frac{4}{3}.\pi.{R_C}^3$, the volume of the core sphere

$V_S = \frac{4}{3}.\pi.\left[(R_C + T_S)^3 - {R_C}^3\right]$, the volume of the FeO_x shell

If $R_C = T_S$, then $V_S = 7.V_C$.

Let us consider the reaction of one core–shell $Fe^0@FeO_x$ particle with Pd^{2+}. One can assume that:

(i) $Fe(OH)_2$ located in the shell is oxidized by Pd^{2+} ions to give Fe_3O_4 and Pd^0 according to the reaction:

$Pd^{2+} + 3\ Fe(OH)_2 + 2OH^- = Pd^0 + Fe_3O_4 + 4\ H_2O$.

(ii) The obtained spherical particle present a Fe^0 core and two shells made of Fe_3O_4 and Pd^0 (Fig. C-1).

(iii) The densities of the various Fe oxides considered here are equal to that of Fe_3O_4.

From assumption (i), $N_{Pd^\circ} = \frac{1}{3}.\%Fe^{II}.N_{Fe}$, with N_{Fe} the number of Fe atoms into the particle, $\%Fe^{II}$ the fraction of Fe atoms in the $Fe(OH)_2$ phase before reaction, and N_{Pd° the number of Pd atoms into the obtained Pd^0 phase after reaction. From assumptions (ii) and (iii), the thickness of the Fe oxide shell remains unchanged (equal T_S) after reaction and N_{Fe} can be calculated as: $N_{Fe} = C_{Fe}.V_C + C_{Fe3O4}.V_S$, with C_{Fe} (0.085 atom $Å^{-3}$) and C_{Fe3O4} (0.041 atom $Å^{-3}$) the concentration of Fe atoms into Fe^0 and Fe_3O_4, respectively.

Therefore, the thickness (T_{Pd°) of the resulting Pd^0 shell can be easily derived from the volume V_{Pd} of the Pd^0 shell given by: $V_{Pd} = \frac{M_{Pd}}{\rho_{Pd^\circ}.\mathcal{N}_A}.N_{Pd^\circ}$, with M_{Pd} the molar mass of Pd (106.4 g mol^{-1}), ρ_{Pd} the density of Pd^0 (12.02 g cm^{-3}), and $\mathcal{N}_A$ the Avogadro constant. It comes:

$$T_{Pd^{\circ}} = \left[(A.\%Fe^{II} + 8)^{1/3} - 2\right].R_C \qquad \text{Eq (C-1)}$$

With A a constant given by: $A = \frac{M_{Pd}}{3.\rho_{Pd^{\circ}}.\mathcal{N}_A}.(C_{Fe} + C_{Fe3O4}.7)$

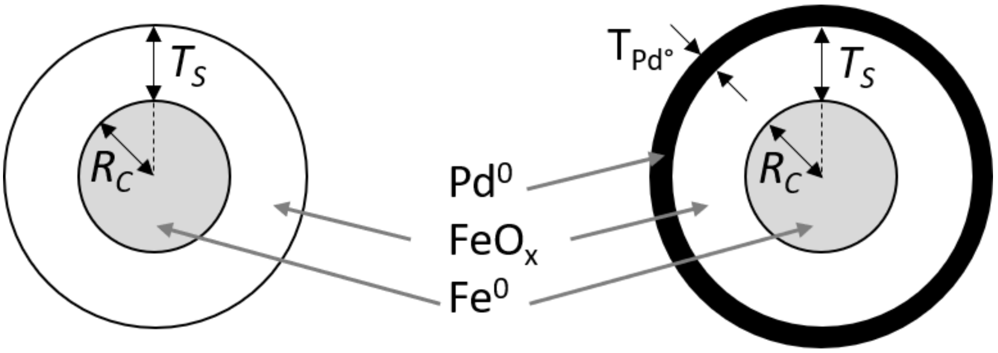

Fig. C-1: Schemes of $Fe^0@FeO_x$ (left) and $Fe^0@FeO_x/Pd^0$ (right) particles.

References

[1] X. Zhao, W. Liu, Z. Cai, B. Han, T. Qian, D. Zhao, An overview of preparation and applications of stabilized zero-valent iron nanoparticles for soil and groundwater remediation, Water Res. 100 (2016) 245–266. https://doi.org/10.1016/j.watres.2016.05.019.

[2] Y. Mu, F. Jia, Z. Ai, L. Zhang, Iron oxide shell mediated environmental remediation properties of nano zero-valent iron, Environ. Sci. Nano 4 (2017) 27–45. https://doi.org/10.1039/C6EN00398B.

[3] C.B. Wang, W.X. Zhang, Synthesizing nanoscale iron particles for rapid and complete dechlorination of TCE and PCBs, Environ. Sci. Technol. 31 (1997) 2154–2156. https://doi.org/10.1021/es970039c.

[4] T. Tosco, M. Petrangeli Papini, C. Cruz Viggi, R. Sethi, Nanoscale zerovalent iron particles for groundwater remediation: a review, J. Cleaner Prod. 77 (2014) 10–21. https://doi.org/10.1016/j.jclepro.2013.12.026.

[5] M. Velimirovic, T. Tosco, M. Uyttebroek, M. Luna, F. Gastone, C. De Boer, N. Klaas, H. Sapion, H. Eisenmann, P.-O.Larsson, J. Braun, R. Sethi, L. Bastiaens, Field assessment of guar gum stabilized

microscale zerovalent iron particles for in-situ remediation of 1,1,1-trichloroethane, J. Contam. Hydrol. 164 (2014) 88–99. https://doi.org/10.1016/j.jconhyd.2014.05.009.

[6] S. Comba, R. Sethi, Stabilization of highly concentrated suspensions of iron nanoparticles using shear-thinning gels of xanthan gum, Water Res. 43 (2009) 3717–3726. https://doi.org/10.1016/j.watres.2009.05.046.

[7] Y. Yao, C. Patzig, Y. Hu, R. W.J. Scott, In situ X-ray absorption spectroscopic study of Fe@FexOy/Pd and Fe@FexOy/Cu nanoparticle catalysts prepared by galvanic exchange reactions, J. Phys. Chem. C 119 (2015) 21209–21218. https://doi.org/10.1021/acs.jpcc.5b06155.

[8] W.-J. Wang, F. Roberts, S. Peterson, S. Ha, L. Scudiero, R. Coustel, M. Mallet, M. Abdelmoula, C. Ruby, Iron-iron oxide supported palladium catalyst for the interconversion of formate and carbon dioxide, Chem. Eng. J. 427 (2022) 131763. https://doi.org/10.1016/j.cej.2021.131763.

[9] E. Wetterskog, C.-W. Tai, J. Grins, L. Bergström, G. Salazar-Alvarez, Anomalous magnetic properties of nanoparticles arising from defect structures: topotaxial oxidation of $Fe_{1-x}O|Fe_{3-\delta}O_4$ core shell nanocubes to single-phase particles, ACS Nano 7 (2013) 7132–7144. https://doi.org/10.1021/nn402487q.

[10] R. Masrour, L. Bahmad, M. Hamedoun, A. Benyoussef, E.K. Hlil, Magnetic properties of Ni/Au core/shell studied by Montecarlo simulations, Phys Lett. A 378 (2014) 276–279. https://doi.org/10.1016/j.physleta.2013.11.012.

[11] Y.-W. Lee, J.-Y. Lee, D.-H. Kwak, E.-T. Hwang, J.I. Sohn, K.-W. Park, Pd@Pt core-shell nanostructures for improved electrocatalytic activity in methanol oxidation reaction, Appl. Catal. B 179 (2015) 178–184. http://doi.org/10.1016/j.apcatb.2015.05.029.

[12] P.B. Santhosh, N.P. Ulrih, Multifunctional superparamagnetic iron oxide nanoparticles: promising tools in cancer theranostics, Cancer Lett. 336 (2013) 8–17. https://doi.org/10.1016/j.canlet.2013.04.032.

[13] X.-Y. Wang, D. Mertz, C. Blanco-Andujar, A. Bora, M. Ménard, F. Meyer, C. Giraudeau, S. Bégin-Colin, Optimizing the silanization of thermally decomposed iron oxide nanoparticles for efficient aqueous phase transfer and MRI applications, RSC Adv. 6 (2016) 93784–93793. https://doi.org/10.1039/C6RA18360C.

[14] R. Hachani, M. Lowdell, M. Birchall, A. Hervault, D. Mertz, S. Begin-Colin, N.T.K. Thanh, Polyol synthesis, functionalisation, and biocompatibility studies of superparamagnetic iron oxide nanoparticles as potential MRI contrast agents, Nanoscale 8 (2016) 3278–3287. https://doi.org/10.1039/C5NR03867G.

[15] C. Blanco-Andujar, A. Walter, C. Bordeianu, D. Mertz, D. Felder-Flesch, S. Bégin-Colin, Design of iron oxide–based nanoparticles for MRI and magnetic hyperthermia, Nanomedicine (Lond) 11 (2016) 1889–1910. https://doi.org/10.2217/nnm-2016-5001.

[16] S.R. Kanel, B. Manning, L. Charlet, H. Choi, Removal of arsenic(III) from groundwater by nanoscale zero-valent Iron, Environ. Sci. Technol. 39 (2005) 1291–1298. https://doi.org/10.1021/es048991u.

[17] Y.-P. Sun, X.-Q. Li, J. Cao, W.-X. Zhang, H. P. Wang, Characterization of zero-valent iron nanoparticles, Adv. Colloid Interface Sci. 120 (2006) 47–56. https://doi.org/10.1016/j.cis.2006.03.001.

[18] A. Mukhtar, X.-M. Cao, T. Mehmood, D.-S. Wang, K.-M. Wu, Structural characterization of self-assembled chain like Fe-FeOx Core shell nanostructure, Nanoscale Res. Lett. 14 (2019) 308. https://doi.org/10.1186/s11671-019-3128-2.

[19] B. Hu, F. Ye, C. Jin, X. Ma, C. Huang, G. Sheng, J. Ma, X. Wang, Y. Huang, The enhancement roles of layered double hydroxide on the reductive immobilization of selenate by nanoscale zero valent iron: macroscopic and microscopic approaches, Chemosphere 184 (2017) 408–416. https://doi.org/10.1016/j.chemosphere.2017.05.179.

[20] S. R. Kanel, J.-M. Greneche, H. Choi, Arsenic(V) removal from groundwater using nano scale zero-valent iron as a colloidal reactive barrier material, Environ. Sci. Technol. 40 (2006), 2045–2050. https://doi.org/10.1021/es0520924.

[21] Z. Chen, X. Tang, W. Qiao, L.A. Puentes Jácome, E.A. Edwards, Y. He, J. Xu, Nanoscale zero-valent iron reduction coupled with anaerobic dichlorination to degrade hexachlorocyclohexane isomers in historically contaminated soil, J. Hazard. Mater. 400 (2020) 123298. https://doi.org/10.1016/j.jhazmat.2020.123298.

[22] A.P. Grosvenor, B.A. Kobe, M.C. Biesinger, N.S. McIntyre, Investigation of multiplet splitting of Fe 2p XPS spectra and bonding in iron compounds, Surf. Interface Anal. 36 (2004) 1564–1574. https://doi.org/10.1002/sia.1984.

[23] M. Mullet, Y. Guillemin, C. Ruby, Oxidation and deprotonation of synthetic Fe^{II}–Fe^{III} (oxy)hydroxycarbonate green rust: an X-ray photoelectron study, J. Solid State Chem. 181 (2008) 81–89. https://doi.org/10.1016/j.jssc.2007.10.026.

[24] L. Néel, Théorie du trainage magnétique des ferromagnétiques en grains fins avec applications aux terres cuites, Annales de Géophysique 5 (1949) 99–136. https://doi.org/10.1051/jphysrad:0195000110204900.

[25] A.M. van der Kraan, Mössbauer effect studies of surface ions of ultrafine α-Fe_2O_3 particles, Phys. Status Solidi A 18 (1973) 215–226. https://doi.org/10.1002/pssa.2210180120.

[26] S. Morup, H. Topsoe, J. Lipka, Modified theory for Mössbauer spectra of superparamagnetic particles: application to Fe_3O_4, J. Phys. Colloques 37 (1976) C6-287–C6-290. https://doi.org/10.1051/jphyscol:1976658.

[27] J. Dormann, D. Fiorani, E. Tronc, On the models for interparticle interactions in nanoparticle assemblies: comparison with experimental results, J. Magn. Magn. Mater. 202 (1999) 251–267. https://doi.org/10.1016/S0304-8853(98)00627-1.

[28] Recoil Software, Ottawa University, K. Lagarec and D. G. Rancourt.

[29] T. Fujii, F.M.F. de Groot, G. A. Sawatzky, F.C. Voogt, T. Hibma, K. Okada, In situ XPS analysis of various iron oxide films grown by NO_2-assisted molecular-beam epitaxy, Phys. Rev. B 59 (1999) 3195–3202. https://doi.org/10.1103/PhysRevB.59.3195.

[30] C. Ruby, J. Fusy, J.-M.R. Génin, Preparation and characterisation of iron oxide films deposited on MgO(100), Thin Solid Films 352 (1999) 22–28. https://doi.org/10.1016/S0040-6090(99)00292-8.

[31] M.P. Seah, W.A. Dench, Quantitative electron spectroscopy of surfaces: a standard data base for electron inelastic mean free paths in solids, Surf. Interface Anal. 1 (1979) 2–11. https://doi.org/10.1002/sia.740010103.

[32] I. Dézsi, Cs. Fetzer, I. Szűcs, B. Degroote, A. Vantomme, T. Kobayashi, A. Nakanishi, Ultrathin Fe layers on Ag (1 0 0) surface, Surf. Sci. 601 (2007) 2525–2531. https://doi.org/10.1016/j.susc.2007.04.202.

[33] C.M. Srivastava, S.N. Shringi, M.V. Babu, Mössbauer study of the low temperature phase of magnetite, Phys. Status Solidi A 65 (1981) 731–735. https://doi.org/pssa.2210650241.

[34] A. Govaert, P. Dauwe, P. Plinke, E. De Grave, J.A. De Sitter, A classification of goethite minerals based on the Mössbauer behavior, J. Phys. Colloque (1976) C6-825–C6-827. https://doi.org/10.1051/jphyscol:19766173.

[35] P.M. Parker, Nuclear quadrupole levels in single crystals, J. Chem. Phys. 24 (1956) 1096–1102.

https://doi.org/10.1063/1.1742686.

[36] H. Myamoto, T. Shinjo, Y. Bando, T. Takada, Mössbauer effect of ^{57}Fe in $Fe(OH)_2$, Bull. Inst. Chem. Res. Kyoto Univ. 45 (1967) 333–341. http://hdl.handle.net/2433/76208.

[37] J.-M.R. Génin, M. Abdelmoula, C. Ruby, C. Upadhay, Speciation of iron: characterization and structure of green rusts and Fe^{II-III} oxhyhydroxycarbonate fougerite, CR Geosci. 338 (2006) 402–419. https://doi.org/10.1016/j.crte.2006.04.005.